Biomechanical Simulation of Lung Deformation from One CT Scan

Feng Li and Fatih Porikli

Abstract We present a biomechanical model based simulation method for examining the patient lung deformation induced by respiratory motion, given only one CT scan input. We model the lung stress-strain behavior using a sophisticated hyperelastic model, and solve the lung deformation problem through finite element (FE) analysis. We introduce robust algorithms to segment out the diaphragm control points and spine regions to carefully define the boundary conditions and loads. Experimental results through comparing with the manually labeled landmark points in real patient 4DCT data demonstrate that our lung deformation simulator is accurate.

1 Introduction

The use of four-dimensional computed tomography (4DCT) has becoming a common practice in radiation therapy, especially for treating tumors in thoracic areas. There are two alternative methods for 4DCT acquisition, namely retrospective slice sorting and prospective sinogram selection. No matter which method is used, the prolonged acquisition time results in a considerably increased radiation dose. For example, the radiation dose of a standard 4DCT scan is about 6 times of that of a typical helical CT scan and 500 times of a chest X-ray. Moreover, 4DCT acquisition cannot be applied to determine the tumor position in-situ. These facts have become a major concern in the clinical application of 4DCT, motivating development of advanced 4DCT simulators.

Towards this goal, various approaches have been proposed to model lung inflation/deflation. The first category of methods discretize the soft tissues (and bones) into masses (nodes) and connect them using springs and dampers (edges) based on

Feng Li
Mitsubishi Electric Research Laboratories, Cambridge, MA 02139, USA.

Fatih Porikli
Mitsubishi Electric Research Laboratories, Cambridge, MA 02139, USA.

mass-spring-damper system and CT scan values for spline-based MCAT phantoms [16], augmented reality based medical visualization [15], respiration animation [23], tumor motion modeling [21], and etc. Conventionally, they apply affine transformations to the control points to simulate respiratory motion. Lungs and body outline are linked to the surrounding ribs, such that they would have the synchronized expansion and contraction [16]. These approaches can only provide approximate deformations.

The second category of methods use hyperelastic models to describe the nonlinear stress-strain behavior of the lung. The straightforward way to simulate lung deformation between two breathing phases (T_i, T_{i+1}) is to use the lung shape at T_{i+1} as the contact/constraint surface and deform the lung at T_i based on the predefined mechanical properties of lung [18, 10]. In this case, a negative pressure load on the lung surface is applied and Finite Element (FE) analysis is used to deform tissues [22]. The lung will expand according to the negative pressure and slide against the contact surface to imitate the pleural fluid mechanism [3]. This pressure can be estimated from the patient's pleural pressure vs. lung volume curve, which in turn are measured from pulmonary compliance test [20]. Along this line, patient-specific biomechanical parameters on the modeling process for FE analysis using 4DCT data are learned in [19]. A deformable image registration of lungs study to find the optimum sliding characteristics and material compressibility using 4DCT data is presented in [1].

Besides lung deformation, the displacements of rib cage and diaphragm are also very important to design a realistic 4DCT simulator. Didier et al. [6] assume the rib cage motion is a rigid transformation and use finite helical axis method to simulate the kinematic behavior of the rib cage. They develop this method into a chest wall model [7] relating the ribs motion to thorax-outer surface motion for lung simulation. Saadé et al. [14] build a simple diaphragm model consisting of central tendon and peripheral muscular fibre. They apply cranio-caudal (CC) forces on each node of the muscular fibre to mimic the diaphragm contraction and use Gauchy-Green deformation tensor to describe the lung deformation. Hostettler et al.[11] consider *internal organs* inside the rib cage as a convex balloon and estimate internal deformation field directly through interpolation of the skin marker motions.

Patient-customized deformation approaches often assume a 4DCT of the patient is already available. We note that simulating deformations without any 4DCT has many challenges as lung motion changes considerably depending on health condition (with or without cancer), breathing pattern (abdomen vs. chest wall), age and many other factors. Nevertheless, 4DCT simulation without any prior (e.g. 4DCT of the same patient) is useful for developing treatment strategy in image-guided radiotherapy and generating controlled data to design and evaluate X-ray video based medical solutions.

In this paper, we present a biomechanical model based thoracic 4DCT simulation method that can faithfully simulate the deformation of lung and nearby organs for the whole breathing cycle. Our method takes only one CT scan as input, and defines the loads on the rib cage and the diaphragm to constrain the lung deformation. This differentiates our method from conventional continuum mechanics based

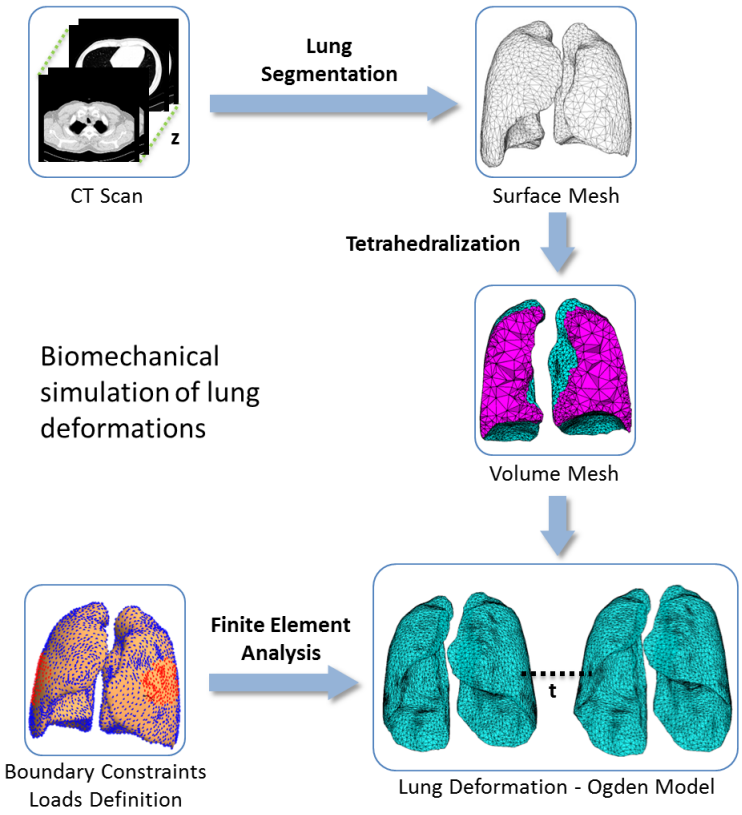

Fig. 1 Processing pipeline of our biomechanical simulation of lung deformations from one CT scan. The tetrahedra on the cutting plane of the volume mesh are colored in purple. Red points indicate imposed automatic boundary constraints.

algorithms. In the extended version of this paper, we also simulate the passive mass-spring model based deformation of abdominal organs due to lung inflation/deflation. Conversion from density to mass assumptions for mass-spring model are supported by clinical data. To evaluate the accuracy of our simulator, we perform both qualitative image visual examination and quantitative comparison on expert annotated lung interior point pairs between multiple breathing phases, and demonstrate that our biomechanical model based simulation is very accurate. Fig. 1 shows the processing pipeline of our 4DCT simulator based on biomechanical model.

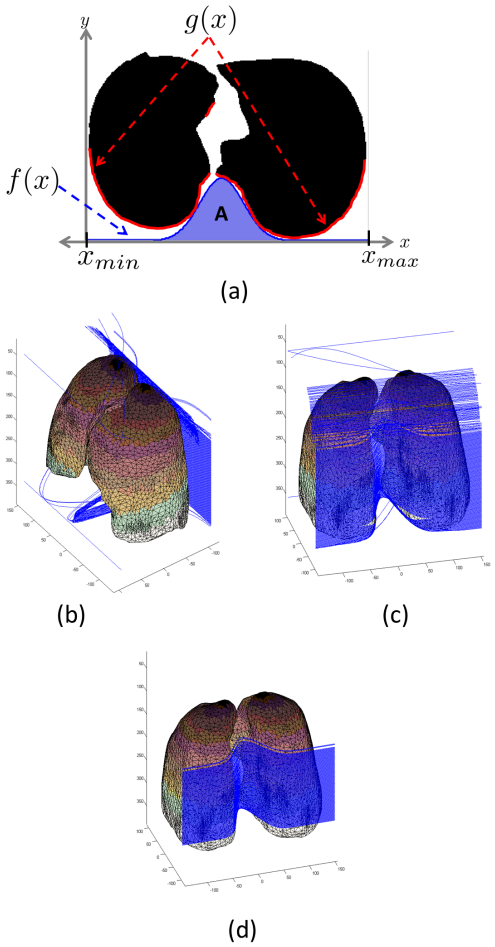

Fig. 2 Gaussian curve fitting for spine region estimation: (a)2D Gaussian curve fitting on a CT slice, (b) and (c) the different views of our 3D curve fitting results, and (d) final curve fitting result after outliers are removed.

2 Methods

2.1 Boundary Constraints Definition

For simplicity of notation, we use x, y, and z to represent lateral, anterioposterior (AP), and superoinferior (SI) direction respectively. Since we do not assume we have a 4DCT of the patient available, it is not possible to use the actual lung surfaces of different breathing phases to define the deformation boundary constraints.

Instead, we define boundary constraints on the lung surface based on the anatomy and function of the human respiratory system [17] for the lung deformation. First, considering that the upper lobes of the lung are well constrained by the ribs, the displacement vectors (x, y and z components) of the tip surface region of upper lobes are fixed to avoid a pure translation of the lung when simulating the diaphragm contracting on the bottom of the lung. We take the clinical study in [9] as a basis for these constraints.

During inspiration, the lung sliding against the rib cage mainly occurs in the posterior/spine region, while in the anterior region, the lung expands with the increasing of thoracic cavity and the relative sliding between them is much smaller [4, 5]. This phenomenon can also be observed in the DIR-Lab 4DCT dataset [2], which is one of the most recent clinical studies with expert annotations for this problem. Therefore, we define the boundary conditions for both the front and the back parts of the lung surface in order to simulate the different sliding actions. As shown in the boundary constraints box of Fig. 1, our system fixes the z displacement for all surface mesh vertices marked in red to simulate the coherent motion of lung with the thorax expansion on the axial plane. The selection of the vertices is based on empirical evidence [2]. These vertices satisfy all these heuristics that they are on/near the convex hull of the lung surface, around the lateral sides of the middle and lower lobes, and have small ($< 20^\circ$) normal variations.

To simulate the pleural sliding in the spine region, our simulator automatically locates the lung surface vertices in the vicinity of the thoracic vertebrae, and fixes the x and y displacements of these points as the third boundary constraint. Notice that our goal is to find surface vertices close to the spine, therefore we design a simple Gaussian curve fitting algorithm to locate these points instead of adopting a complicated thoracic vertebrae segmentation approach. The idea is to fit a set of Gaussian curves such that the area cut out by each curve is maximized. This provides a good global approximation to the spine shape and the constraint points can be accurately located. For simplicity, considering a sample 2D axial view, our algorithm maximizes the light blue region A covered by the blue Gaussian curve $f(x) = ae^{-\frac{(x-b)^2}{2c^2}}$, as shown in Fig. 2(a).

We formulate it as a constrained multi-variable optimization problem as :

$$\max_{a,b,c} \sum_{x=x_{min}}^{x_{max}} f(x), \quad \text{s.t. } f(x) - g(x) \leq 0, \forall x \in [x_{min}, x_{max}], \tag{1}$$

where the parameter a, b and c represent the scaling factor, expected value, and standard variance of $f(x)$, x_{min} and x_{max} are the lung limits in the lateral direction, and $g(x)$ is the upper limit for $f(x)$ and is the minimum y value of the lung slice at each x. In our simulator, this constrained optimization problem is solved very efficiently by a sequential quadratic programming method, specifically active-set algorithm, which computes a quasi-Newton approximation to the Hessian of the Lagrangian at each iteration. We extend this 2D algorithm to the 3D CT volume by simply applying this algorithm slice by slice, as can be seen in Fig. 2 (b) and (c). Outliers occur in the top and bottom of the lung where $g(x)$ is only partial

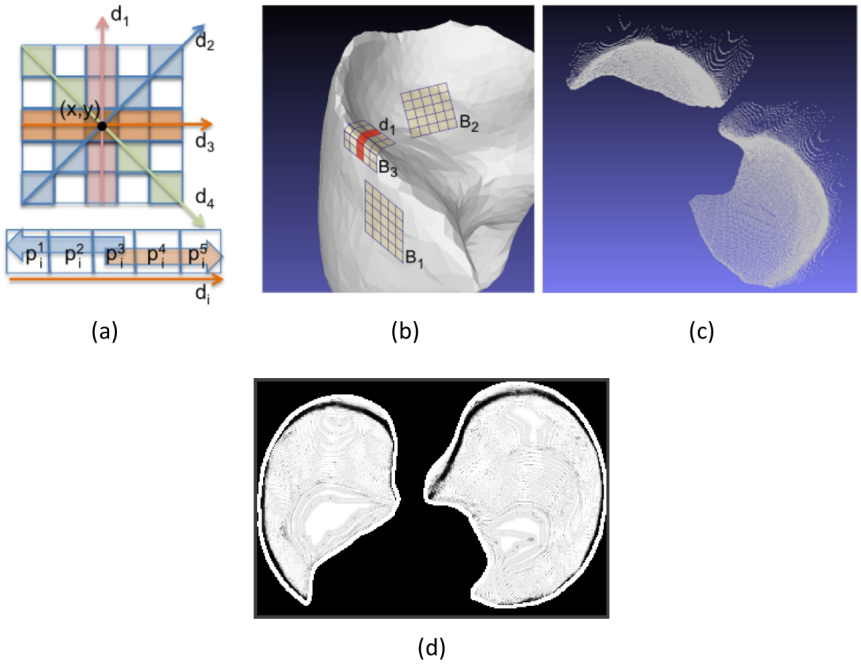

Fig. 3 Weight map calculation for diaphragm point segmentation. (a) The line direction definition of our LDD measure. (b) Sample blocks on the lung surface to illustrate our weight calculation algorithm. The orange region d_1 of B_1 has the highest LDD value out of the three sample blocks. (d) The weight map corresponding to the input point cloud (c).

constraints for the curve fitting. Our simulator removes these outliers by computing their difference to the mean Gaussian curve of the set, therefore correct fittings of the thoracic vertebrae are retained. The missing curves can be estimated by linear interpolation of the remaining curves.

2.2 Loads Definition

Since we are given one input CT scan and there is no bounding surface at the second breathing phase, we design an extra traction applied on the diaphragm area of the lung besides the negative intra-pleural surface pressure. The pressure force inflates the lung in all directions during inspiration, while the traction allows additional displacement in z direction to mimic the diaphragm contraction and pleural sliding.

Note that the pressure force can be well defined from the simulator input, therefore we focus on how to accurately locate the points (faces) that are close to the diaphragm for the definition of the traction. We model this as a graph search problem and solve it by our modified shortest closed-path algorithm. Our simulator first

computes a dense 3D point cloud by finding the lung voxels at every (x,y) location with the largest z value, as shown in Fig. 3(c), then converts the point cloud into a weight map, Fig. 3(d), based on the local geometry information, and finally locates the diaphragm points (Fig. 4(f)) through our modified shortest closed-path algorithm. The left and right lower lobe are treated separately.

Weight Map Definition: We consider the 3D point cloud as an 2D image with intensity value from the z value of the corresponding point, and run the local Line Direction Discrepancy (LDD) computation on this image to generate the weight map W. Thus our weight map computation can also be viewed as a special type of image filtering. As shown in Fig. 3(a), for each line $d_i(x,y)$ of a block centering at (x,y), we build up two sub-lines $d_i^1(x,y)$ and $d_i^2(x,y)$ from (p_i^3, p_i^2, p_i^1) and (p_i^3, p_i^4, p_i^5) respectively, $(i = 1,\ldots,4)$, and compute the LDD as the minimum intersection angle of the four sub-line pairs. Alternatively, we compute the maximum of the cosine value of these angles to represent the weight, which can be efficiently calculated through dot product as

$$W(\mathbf{p}) = \max_{i=1,\ldots,4} \{ \frac{d_i^1 \cdot d_i^2}{\| d_i^1 \| \cdot \| d_i^2 \|} \} , \tag{2}$$

where $\mathbf{p}$ represents pixel position (x,y), and the block size is set as 5×5 for simplicity. Intuitively, regions with high curvature would high/positive LDD value, for example, d_1 of B_3 in Fig. 3(b), while flat regions would have low/negative LDD values, for instance, B_1 and B_2.

Diaphragm Point Segmentation: Notice that all outliers locate at the boundary of the weight map, thus we formulate the diaphragm point segmentation as a shortest closed-path (SCP) problem, which finds a optimal cut along the boundary that separates the diaphragm points from the outliers. To build the graph for SCP, we choose 4 neighborhood connection and set the edge weight $E_{\mathbf{pq}}$ as $W(\mathbf{q})$. Therefore, $E_{\mathbf{pq}}$ and $E_{\mathbf{qp}}$ may have different weights. Instead of using the entire weight map to build the graph, we mask out the inner region through morphological operations and limit the optimal cut (red curve) between the inner $\partial\Omega_2$ and outer boundary $\partial\Omega_1$ (blur curves), as shown in Fig. 4(a). If we directly adopt the idea from [12] to design the SCP algorithm, some interior regions would be inevitably cut out to favor the lowest cost, as shown in Fig. 4 (b) and (c).

To solve this problem, we first sample the outer boundary $\partial\Omega_1$ every 10 points and find their corresponding points (in terms of Euclidean distance) on the inter boundary $\partial\Omega_2$, as the green lines shown in Fig. 4(d). For the rest points on $\partial\Omega_1$, we compute their matches on $\partial\Omega_2$ (purple lines) through linearly interpolation of the previous matches (green lines), such that there are no crossing matches (lines) and correct ordering could be maintained. In this way, we can unbend the ring region between $\partial\Omega_1$ and $\partial\Omega_2$ into a ribbon belt by aligning up all the purple and green lines in order, and set the length of the ribbon as the length of $\partial\Omega_1$ and the width as the shortest distance between $\partial\Omega_1$ and $\partial\Omega_2$. We then build up a new adjacency matrix/graph from the ribbon for the SCP algorithm. As we can see from Fig. 4(e-f), this would give us the accurate diaphragm points for the traction definition.

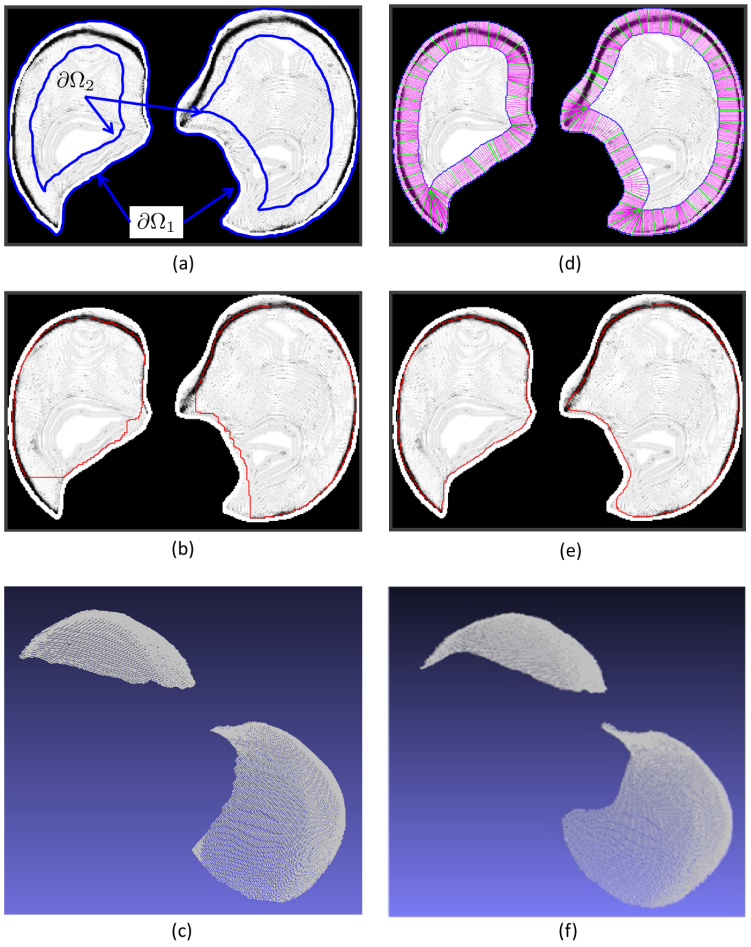

Fig. 4 Diaphragm point segmentation. (a) Masked out the inner region: the inner $\partial\Omega_2$ and outer boundary $\partial\Omega_1$ (blue curves). (b) The optimal cut by conventional SCP algorithm (in red). (c) The estimated diaphragm points. Our new SCP algorithm unbends the ring regions in (d) into ribbon belts, and can accurately segment out the diaphragm points for traction definition in (e) and (f).

2.3 Finite Element Simulation

The final step for biomechanical simulation of lung deformation is to define the material property of the lung and apply FE analysis. We assume the lung tissue is homogeneous, isotropic, and use the first-order Ogden model [13] to describe its non-linear strain energy density function as

$$W(\lambda_1,\lambda_2,\lambda_3,J) = \frac{\mu_1}{\alpha_1}(\lambda_1^{\alpha_1}+\lambda_2^{\alpha_1}+\lambda_3^{\alpha_1}-3)+\frac{K}{2}(\ln J)^2\,, \tag{3}$$

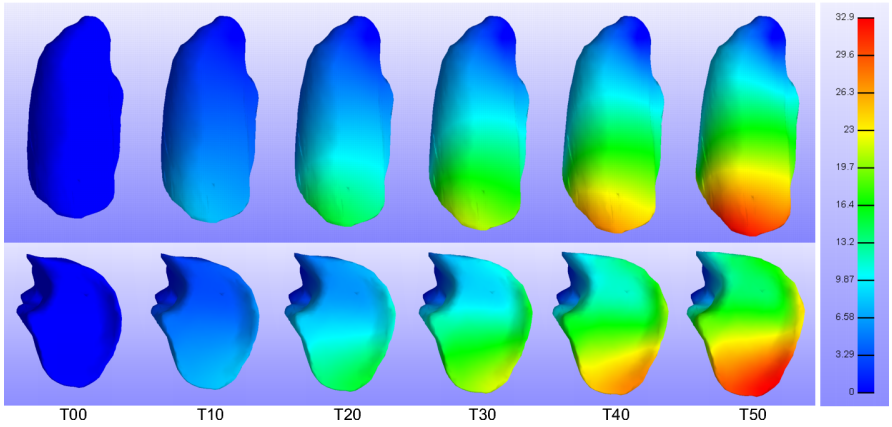

Fig. 5 Finite element analysis of a left lung deformation during inspiration. The top row displays the posterior view and the bottom row shows the inferior view. Color shows the degree of displacement with red denoting maximum displacement.

where $\lambda_{1,2,3}$ are the deviatoric principal stretches, μ_1 and α_1 are material constants, J is the Jacobian of the lung deformation, and K is the bulk modulus chosen sufficiently high to satisfy near-incompressibility. Here, we choose the Ogden parameters from [8] for all our experiments, $\mu_1 = 0.0329$, and $\alpha_1 = 6.82$.

Next, we combine all the information (meshes, loads, and boundaries) defined in the previous sections into a single script file and directly run a FE solver to simulate the lung deformation. We integrate the open-source FEBio [8] into our simulator as the FE solver, and a lung deformation example is shown in Fig. 5.

3 Results and Discussion

Figure 5 shows an example of FE analysis of a left lung deformation during inspiration. The simulation results resemble the real 4DCT lung deformation with the maximum displacement occurring in the posterior region along the SI direction. The results also demonstrate realistic lung inflating effect due to the negative surface pressure, which can be better viewed in the second row of the figure. In our FE analysis, we define the simulation time for the inspiration phase is 2 seconds with step size $\Delta t = 0.1$, pressure force -0.02 and traction 0.005. For other parameters, for example, convergence tolerance, we use the default values in the FEBio solver.

To demonstrate the accuracy of our FE simulation, we evaluate our simulator on the DIR-Lab 4DCT dataset [2]. We use the cases with 512×512 slice resolution. Each test case has 300 manually labeled landmark points between T_{ex} and T_{in}. For instance, *case-7*, which has an average landmark displacement of 11.59 ± 7.87 (standard deviation) mm, and the observer error of 0.81 ± 1.32 mm. Detailed specifications of the dataset can be found at http://www.dir-lab.com.

In our experiments, we compute the error as the Euclidean distance between our simulated displacement vectors and the manually labeled ones. We also implement the deformation filed estimation algorithm proposed by Hostettler et al. [11], and set its model parameters using the ground-truth marker displacement vectors. We compare its simulation results with ours in Tab. 1, and the detailed distributions of simulation errors for *case-7* in Fig. 6. From the table, we can see that the accuracy of our simulator improves roughly 40% compared with [11]. The reasons why our simulator has larger errors in z direction are twofold. First, human lung generally has strong respiratory motions in this direction. And more importantly, the CT volume data has stronger artifacts and lower resolution in z than x and y, considering that the spatial resolution of tested CT data is $0.97 \times 0.97 \times 2.5$ mm.

We compute the error as the Euclidean distance between the simulated displacement vectors and the manually labeled ones. In Fig. 7, we show the comparison between our FE analysis results and the ground-truth displacement vectors for *case-7*. For better illustration, we only show the left lung, which has 153 landmark points.

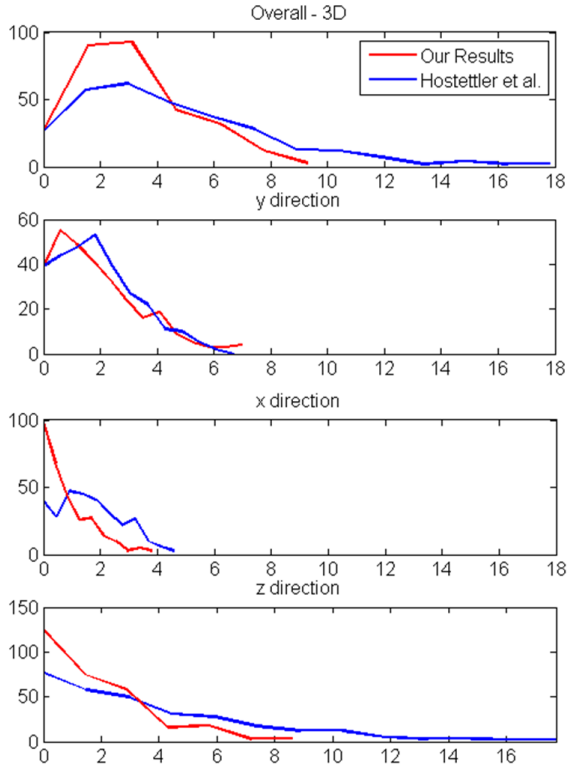

Fig. 6 Mean error distributions of our simulation results and Hostettler et al. [11] for overall 3D, and in x, y, and z directions for *case7*. Horizontal axes are the error magnitudes in *mm*. As visible, our simulator has more accurate estimation.

Case ID	CT Dims	Our Results	Hostettler et al.[11]
case7	512×512×136	3.79 (1.80)	5.31 (3.35)
case8	512×512×128	6.15 (3.31)	10.81 (4.69)
case9	512×512×128	3.17 (1.37)	5.86 (1.83)
case10	512×512×120	4.37 (2.95)	6.93 (2.86)

Table 1 Mean error (and standard deviation) of the deformed lungs measured in 3D space and its x, y, and z components in *mm*. This table demonstrates that our biomechanical simulation algorithm for lung deformation is accurate and performs better than [11] on tested DIR-Lab 4DCT datasets [2].

It can be seen that our simulator generates accurate results in the lower posterior region where the nodal displacement is mostly prominent. We observe that our simulation results have some angular difference with the manually labeled data in the upper anterior region. That is partially due to lack of other prior force definitions for these elements in the simulator as it only uses the negative surface pressure. Besides, it is possible that the manually identified landmark points contain large errors since nodal displacement in this region is less than or around the z spatial resolution of the CT dataset.

We implement the deformation filed estimation algorithm proposed by Hostettler et al. [11], and set its model parameters using the ground-truth marker displacement vectors. We compare its simulation results with ours in Table 1. From the table, we can see that the accuracy of our simulator improves roughly 40% compared with [11]. As indicated by [2], these test cases have very different patient lung shapes, tumor sizes and locations, and breathing mechanisms. A simple interpolation between axial lung envelopes adopted by Hostettler et al. [11] inevitably generates large errors while our algorithm adapts to different patients, thus achieves comparably more accurate results as shown in Table 1.

Our algorithm is a patient-customized lung deformation simulator. By providing more sophisticated constraints, the simulation quality will improve further. For instance, the patient lung surface in *case-8* is heavily curved in the back/posterior region, thus including extra constraints to maintain this curved lung shape may make the simulation more precise.

4 Conclusions

We have present a biomechanical model based lung simulation method for examining the patient lung deformation induced by respiration given only one CT scan input. We model the lung stress-strain behavior using a hyperelastic model, and simulate the lung deformation by defining accurate boundary constraints and loads. Extensive analysis and comparisons with the manually labeled DIR-Lab dataset demonstrate that our lung deformation results are accurate.

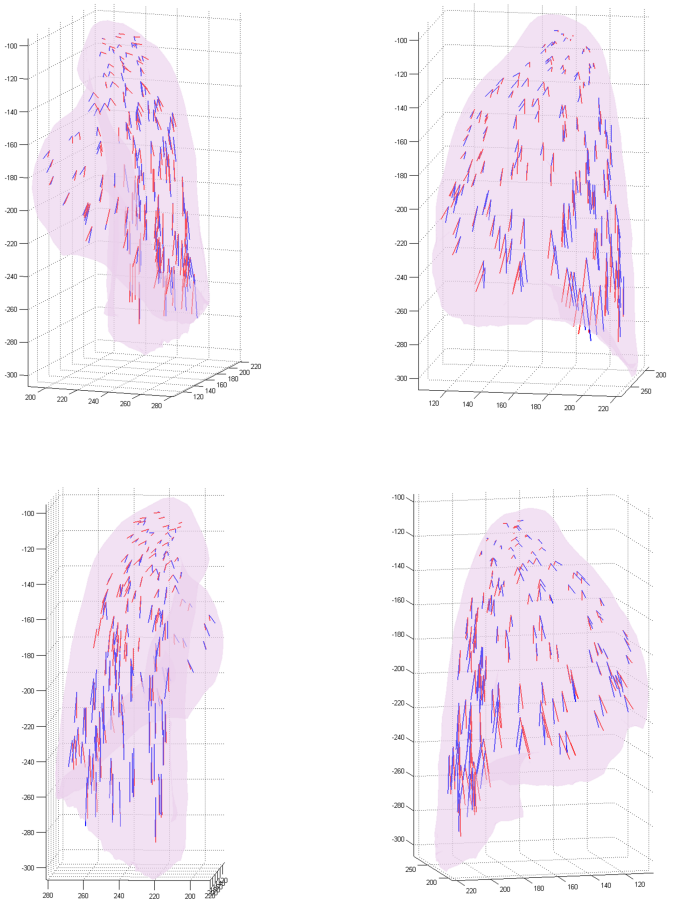

Fig. 7 Comparison between our simulated displacement vectors and ground-truth data at manually identified landmark positions for *case-7*. The blue lines represent the ground truth displacement of the landmark points between T_{ex} and T_{in}, while the red lines represent our simulation results.

References

1. A. Al-Mayah, J. Moseley, M. Velec, and K. Brock. Sliding characteristic and material compressibility of human lung: parametric and verification. *Medical Physics*, 36(10):4625–4633, 2009.
2. R. Castillo, E. Castillo, R. Guerra, V. Johnson, T. McPhail, A. Garg, and T. Guerrero. A framework for evaluation of deformable image registration spatial accuracy using large landmark point sets. *Physics in Medicine and Biology*, 54:1849, 2009.
3. E. DiAngelo, S. Loring, M. Gioia, M. Pecchiari, and C. Moscheni. Friction and lubrication of pleural tissues. *Respiratory physiology & neurobiology*, 142(1):55–68, 2004.
4. S. Zuckerman. A New System of Anatomy. *Oxford University Press*, 1963.

5. W. Norman. The Anatomy Lesson. *Georgetown University*, 1999.
6. A. Didier, P. Villard, J. Bayle, M. Beuve, and B. Shariat. Breathing thorax simulation based on pleura physiology and rib kinematics. *IEEE International Conference on Medical Information Visualisation-BioMedical Visualisation*, 2007.
7. A. Didier, P. Villard, J. Saadé, J. Moreau, M. Beuve, and B. Shariat. A chest wall model based on rib kinematics. In *IEEE International Conference on Visualisation*, 2009.
8. B. Ellis, G. Ateshian, and J. Weiss. FEBio: Finite elements for biomechanics. *Journal of Biomechanical Engineering*, 134(1):5–11, 2012.
9. J. Ehrhardt, R. Werner, T. Frenzel, W. Lu, D. Low, and H. Handels. Analysis of free breathing motion using artifact reduced 4DCT image data. *SPIE Medical Imaging Conference*, 2007.
10. J. Eom, C. Shi, X. Xu, and S. De. Modeling respiratory motion for cancer radiation therapy based on patient-specific 4DCT data. *MICCAI*, 2009.
11. A. Hostettler, S. Nicolau, C. Forest, L. Soler, and Y. Remond. Real time simulation of organ motions induced by breathing: First evaluation on patient data. *Biomedical Simulation Conference*, 2006.
12. J. Jia, J. Sun, C. Tang, and H. Shum. Drag-and-drop pasting. *ACM SIGGRAPH Conference*, 2006.
13. R. Ogden. Large deformation isotropic elasticity-on the correlation of theory and experiment for incompressible rubberlike solids. *Proceedings of the Royal Society of London. Series A, Mathematical and Physical Sciences*, 326(1567):565–584, 1972.
14. J. Saadé, A. Didier, P. Villard, R. Buttin, J. Moreau, M. Beuve, and B. Shariat. A preliminary study for a biomechanical model of the respiratory system. *International Conference on Computer Vision Theory and Applications*, 2010.
15. A. Santhanam, C. Fidopiastis, F. Hamza-Lup, J. Rolland, and C. Imielinska. Physically-based deformation of high-resolution 3d lung models for augmented reality based medical visualization. *Medical Image Computing and Computer Aided Intervention, AMI-ARCS*, pages 21–32, 2004.
16. W. Segars, D. Lalush, and B. Tsui. Modeling respiratory mechanics in the MCAT and spline-based MCAT phantoms. *IEEE Transactions on Nuclear Science*, 48(1):89–97, 2001.
17. B. Vidiâc and F. Suarez. *Photographic atlas of the human body*. CV Mosby (St. Louis), 1984.
18. P. Villard, M. Beuve, B. Shariat, V. Baudet, and F. Jaillet. Simulation of lung behaviour with finite elements: influence of biomechanical parameters. *IEEE International Conference on Medical Information Visualisation-Biomedical Visualisation*, 2005.
19. R. Werner, J. Ehrhardt, R. Schmidt, and H. Handels. Patient-specific finite element modeling of respiratory lung motion using 4DCT image data. *Medical Physics*, 36(5):1500–1511, 2009.
20. J. West. *Respiratory physiology: the essentials*. Lippincott Williams & Wilkins, 2008.
21. P. Wilson and J. Meyer. A spring–dashpot system for modelling lung tumour motion in radiotherapy. *Computational and Mathematical Methods in Medicine*, 11(1):13–26, 2010.
22. T. Zhang, N. Orton, T. Mackie, and B. Paliwal. Technical note: A novel boundary condition using contact elements for finite element based deformable image registration. *Medical Physics*, 31(9):2412?2415, 2004.
23. V. Zordan, B. Celly, B. Chiu, and P. DiLorenzo. Breathe easy: model and control of simulated respiration for animation. *Graphical Models*, 68(2):113-132, 2006.